Observation of gauge field induced non-Hermitian helical spin skin effects

Yi Li,[1] Jia-Hui Zhang,[1] Yang Kou,[1] Liantuan Xiao,[1,2] Suotang Jia,[1,2] Linhu Li,[3,*] and Feng Mei[1,2,†]

[1] *State Key Laboratory of Quantum Optics Technologies and Devices, Institute of Laser Spectroscopy, Shanxi University, Taiyuan, Shanxi 030006, China*
[2] *Collaborative Innovation Center of Extreme Optics, Shanxi University, Taiyuan, Shanxi 030006, China*
[3] *Quantum Science Center of Guangdong-Hong Kong-Macao Greater Bay Area (Guangdong), Shenzhen, China*

Contents

Supplementary Note 1: Non-Hermitian spin skin effects varying with gauge fields

To better illustrate the influence of the gauge field on the non-Hermitian skin effect, we present energy spectra varying with gauge field phase θ in Fig. S1 and analyze the corresponding density distribution in Fig. S2. In Fig. S1(a), the blue, purple, and orange dots represent the energy spectra under x-PBC and y-PBC, x-PBC and y-OBC, and x-OBC and y-OBC, respectively. When the system is under x-PBC and y-OBC, edge modes emerge within the complex-energy gap and are localized at the boundaries. These edge modes form an enclosed region, except at $\theta = 0$, suggesting the presence of corner skin effects under open boundary conditions. For gauge field phase $\theta \neq \pm\pi$, the gauge field breaks Kramers degeneracy of the edge modes. As the gauge field phase increases from $-\pi$ to 0, the enclosed region shrinks, indicating a weakening of the edge skin effects. However, as θ increases from 0 to π, the enclosed region expands again, signaling the re-emergence and strengthening of the edge skin effects. This behavior suggests a non-monotonic relationship between the gauge field phase and the strength of skin effect, where the system undergoes a reversal in trend after passing through $\theta = 0$. For further illustrate the evolution of the bulk skin effects, we present a redisplay of the partial energy spectra under x-PBC and y-OBC in Fig. S1(b). The arrows indicate the winding direction of the energy bands as a function of k_x, which imply the direction of the skin effects. For $\theta \neq 0, \pm\pi$, the bulk energy bands form a figure-eight-shaped enclosed region, a hallmark of the bulk skin effects. The size of this enclosed region expands as θ increases from $-\pi$ to -0.5π and from 0 to 0.5π, indicating a strengthening of the non-Hermitian bulk skin effects. Conversely, as θ varies from -0.5π to 0 and from 0.5π to π, the enclosed region decreases, signifying a restoration and weakening of the bulk skin effects. Notably, the energy band winding direction reverses at $\theta \in (-\pi, 0)$ and $\theta \in (0, \pi)$ for both edge and bulk bands, implying a corresponding reversal of the skin effect direction, further underscoring its intricate dependence on the gauge field phase. This transition is crucial for understanding the complex interplay between the gauge field phase and skin effect, revealing the system's sensitive dependence on gauge field configuration.

Fig. S2 presents the density distribution $\sum |\psi_n|^2$ for both bulk and edge eigenmodes. By visualizing both the bulk and edge density distribution, we confirm that the system exhibits no skin effect in the absence of a gauge field. When the gauge field phase $\theta \in [0, \pm\pi]$, the system displays a hybrid-order spin skin effect, where both edge and bulk

*Electronic address: lilinhu@quantumsc.cn
†Electronic address: meifeng@sxu.edu.cn

skin effect coexist. At $\theta = \pm\pi$, the system transitions to a second-order spin skin effect, characterized by edge modes localization at the system's corners. We observed variations in the intensity of the skin effect and a reversal in its direction after the gauge field phase flipped, both aligning with our previous analysis. These findings underscore the critical role of the gauge field in governing the intensity and direction of the non-Hermitian skin effect.

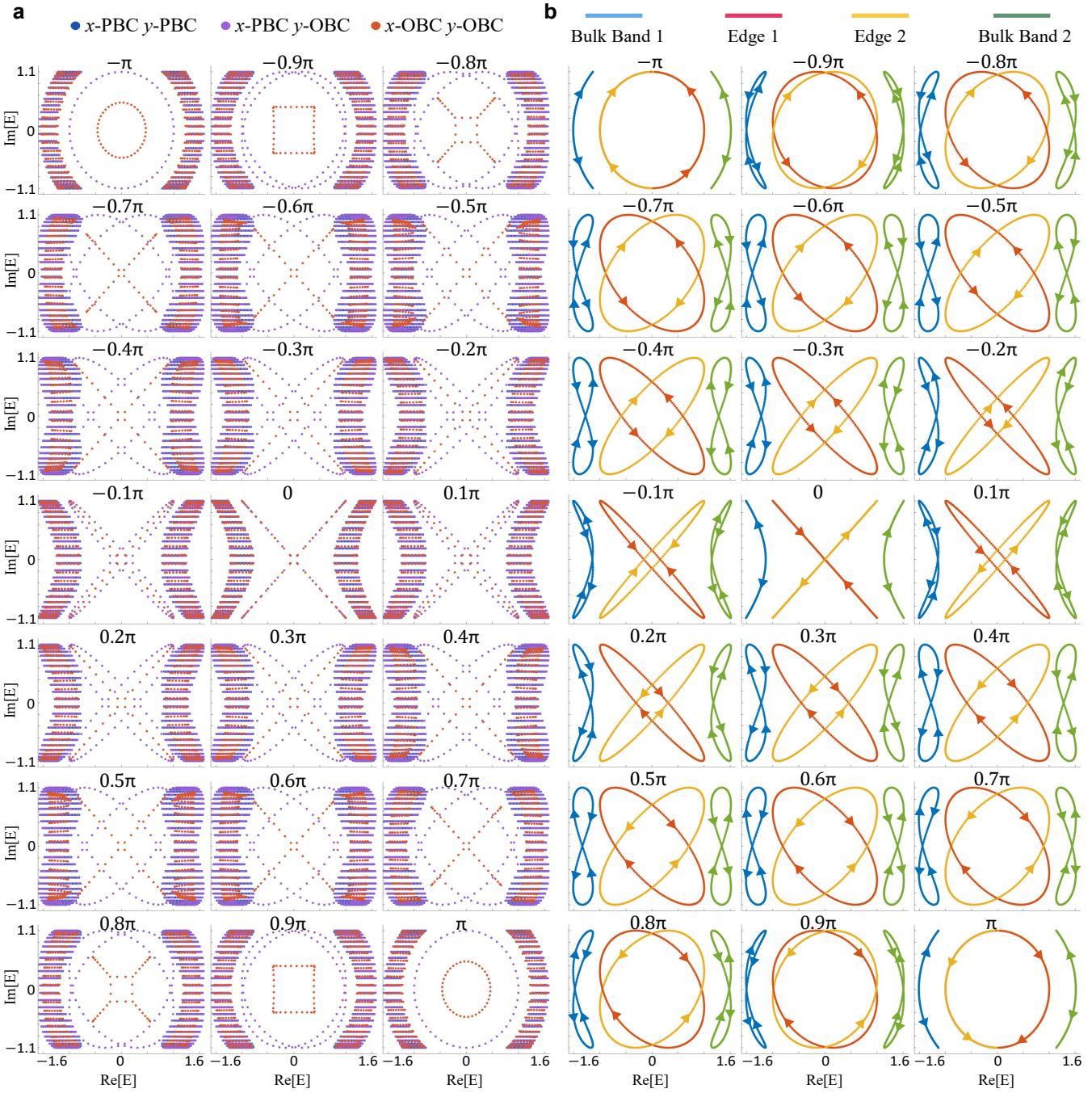

FIG. S1: (a) Complex energy spectra for different gauge field phases under three types of boundary conditions. (b) Energy spectra under x-PBC and y-OBC, where the arrows represent the directions of the complex energy variation with k_x for the bulk and edge bands. The parameters used are the same as those in the main text, with a system size of 20×10.

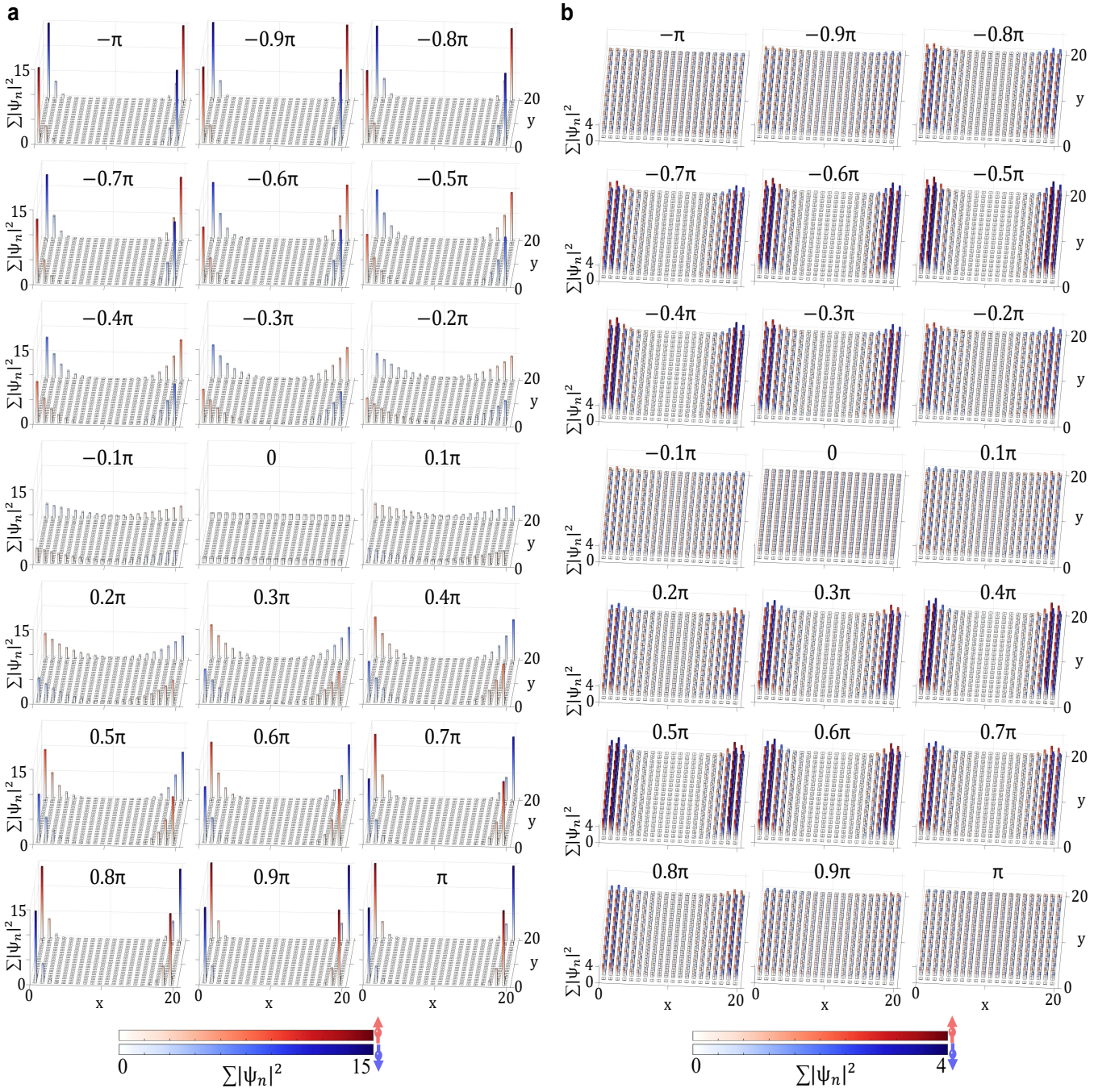

FIG. S2: The (a) edge and (b) bulk modes density distribution varying with gauge field phase, where the red and blue color bars represent spin-up and spin-down modes, respectively.

Supplementary Note 2: Gauge field enabled spinful non-Hermitian topological phases

In this section, we will prove that the application of gauge fields could switch trivial spinless non-Hermitian topological phases into nontrivial spinful non-Hermitian topological phases. This feature can be seen from the transition of time reversal symmetry (TRS). TRS plays a crucial role in topological classification, systems with TRS fall into two distinct classes based on the action of the time-reversal operator T: (i) Spinless systems ($T^2 = 1$), typical for bosonic systems or spinless fermions; (ii) Spinful systems ($T^2 = -1$), for spin-1/2 fermionic systems. These two classes support fundamentally different topological phases.

In our work, the time-reversal symmetry is defined as $T = \mathcal{M}_z KI$, where $\mathcal{M}_z$ is mirror symmetry inverting the z-axis, I represents momentum inversion, and K denotes complex conjugation. A key finding is that the gauge field phase $\theta = 0, \pm\pi$ can significantly impact the system's symmetry properties and topological classification. We start from analyzing the symmetry of intra-layer couplings with 0 and π gauge field phases, as shown in Fig. S3. Under the mirror reflection $M_z = \sigma_x\tau_0$, the two plaquettes behaviors differ significantly. For gauge field phases 0 case (Fig. S3(a)), the intra-layer couplings remains unchanged under mirror reflection M_z, so the mirror symmetry is simply $\mathcal{M}_z = M_z$, leading to the time-reversal operation $T^2 = (\sigma_x\tau_0 KI)(\sigma_x\tau_0 KI) = 1$, corresponding to a spinless system. However, for the gauge field phases π, the mirror operation transforms the intra-layer couplings into a distinct configuration (Fig. S3(b)), meaning that the gauge connection differs under symmetry transformations. These two configurations are related by a gauge transformation $G = i\sigma_z\tau_0$. As a result, the mirror symmetry for the gauge field phases π plaquette is modified to $\mathcal{M}_z = GM_z = -\sigma_y\tau_0$. Importantly, due to the commutation relation $\{G, K\} = 0$ and $[M_z, K] = 0$, the TRS satisfies $T^2 = (-\sigma_y\tau_0 KI)(-\sigma_y\tau_0 KI) = -1$. This signifies a transition to spinful system, where Kramers degeneracy emerges, fundamentally altering the system's topological nature. Our analysis demonstrates that the gauge field phase can induce a transition between topological spin classes: When $\theta = 0$, the system belongs to a spinless topological class ($T^2 = 1$); When $\theta = \pi$, the system transitions to a spinful topological class ($T^2 = -1$).

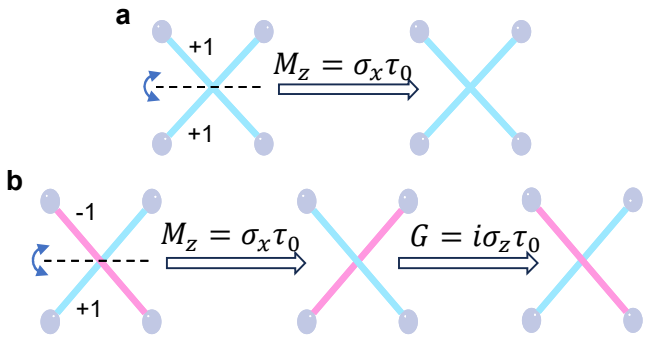

FIG. S3: Schematic illustration of the projective mirror reflection for gauge field phases (a) 0 and (b) π

Supplementary Note 3: Implementation of gauge fields in circuit metamaterials

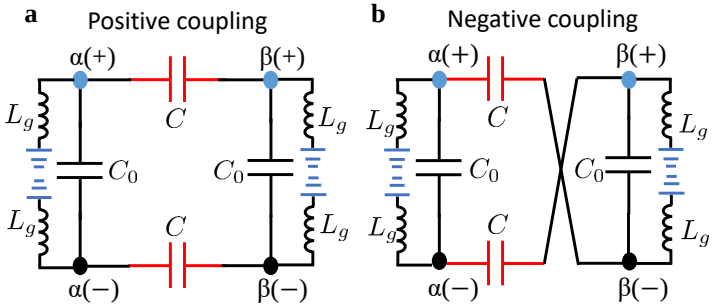

FIG. S4: Two circuit configurations with a two subnode structure. (a) The normal connection, and (b) the one-shift connection. Each subnode ($+$ or $-$) at each node (α or β) is grounded via inductance L_g.

In this section, we show how to implement the arbitrary gauge field phase in circuit metamaterials. The voltage and current at a node can be defined up to a phase factor, which allows the node structure to be enriched by including more subnodes within the same node, where the voltage and current magnitudes remain the same but the phase factors are shifted relative to each other. We start with the node have two subnodes ($\pm$) at which the voltages are shifted by a relative phase factor $\exp(i\pi) = -1$. Two configurations of connection between the neighboring nodes, shown in Fig. S4, the Laplacian matrix can be given by

$$\begin{aligned} J_1(\omega) &= -i\omega[\sigma_0 \otimes \hat{D} + \sigma_x \otimes \hat{C}_1], \\ J_2(\omega) &= -i\omega[\sigma_0 \otimes \hat{D} + \sigma_x \otimes \hat{C}_2], \end{aligned} \tag{1}$$

where $\hat{C}_1 = C\tau_0$, $\hat{C}_2 = C\tau_x$. J_1 (J_2) corresponds to the circuit metamaterials in Fig. S4(a) (Fig. S4(b)), and $\otimes$ represents direct product. The Pauli matrices $\{\sigma_v\}$ and $\{\tau_v\}$ act on the node and the subnode spaces, respectively. Here, the diagonal part in the node space

$$\hat{D} = (\frac{1}{\omega^2 L_g} - C_0 - C)\tau_0 + C_0\tau_x. \tag{2}$$

To determine the hopping and on-site potential, the subnode matrix is projected onto the relevant subnode subspace spanned by the vector $\hat{v} = 1/\sqrt{2}[1, -1]^T$. The projector onto this subspace $\hat{P} = \hat{v}\hat{v}'$ explicitly reads

$$\hat{P} = \frac{1}{2}(\tau_0 - \tau_x). \tag{3}$$

Consequently, the hopping matrix element for the two configurations in Fig. S4 respectively read

$$\begin{aligned} t_1 &= \mathrm{Tr}(\hat{P}\hat{C}_1\hat{P}) = C, \\ t_2 &= \mathrm{Tr}(\hat{P}\hat{C}_2\hat{P}) = -C. \end{aligned} \tag{4}$$

On the other hand, the on site potential for thses two configurations are

$$\mu = \mathrm{Tr}(\hat{P}\hat{D}\hat{P}) = \frac{1}{\omega^2 L_g} - 2C_0 - C. \tag{5}$$

Finally, extending the above construction to more than two subnodes per node allows for the realization of an arbitrary gauge field phase factor.

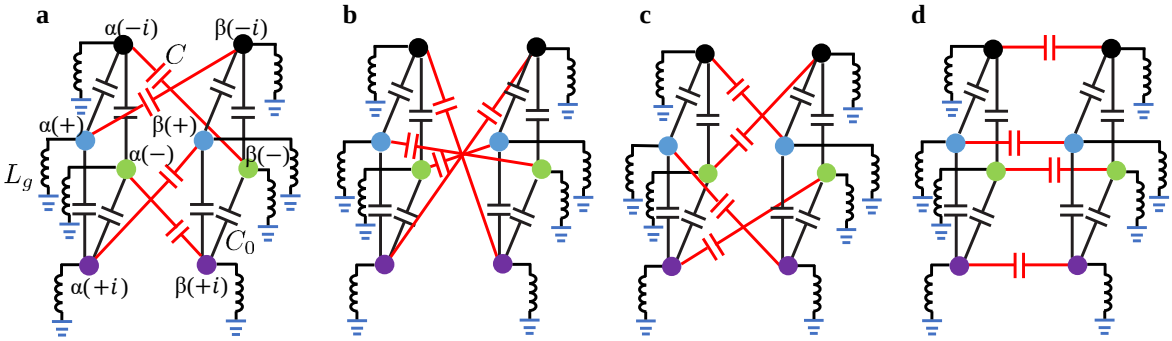

FIG. S5: (a) Schematic representation of the one-shift capacitor connection, where circuit construction of a node with four subnodes $\alpha(\gamma)$, where $\gamma = \pm 1, \pm i$ denote the relative phase of the current or voltage between the subnodes. Two-shift, three-shift, and no-shift or direct capacitor connections between nodes α and β are schematically shown in (b), (c), and (d), respectively. The effective hopping elements between these two nodes or sites are then $t_a = iC$, $t_b = -C$, $t_c = -iC$ and $t_d = C$.

Next we consider the four subnode configurations, as shown in Fig. S5, where the phase differences between the subnode $\alpha(+)$ and the rest of the subnodes (including the subnode $\alpha(+)$) are ± 1, $\pm i$. Therefore the relevant subnode subspace is spanned by the vector $\hat{v} = \frac{1}{2}[1, -i, -1, i]^T$ as shown in Fig. S5(a). The corresponding projector $\hat{P} = \hat{v}\hat{v}'$ explicit form given by

$$\hat{P} = \frac{1}{4}\begin{pmatrix} 1 & i & -1 & -i \\ -i & 1 & i & -1 \\ -1 & -i & 1 & i \\ i & -1 & -i & 1 \end{pmatrix}. \tag{6}$$

The hopping element between the nodes α and β is obtained by projecting the connectivity matrix of the subnodes onto the subspace spanned by the vector $\hat{v}$, namely

$$t_\gamma = \mathrm{Tr}(\hat{P}\hat{C}_\gamma\hat{P}), \tag{7}$$

with $\hat{C}_\gamma$ as the connectivity matrices for the four possible configurations shown in Fig. S5, the corresponding connectivity matrices are

$$\hat{C}_a = \begin{pmatrix} 0 & 0 & 0 & C \\ C & 0 & 0 & 0 \\ 0 & C & 0 & 0 \\ 0 & 0 & C & 0 \end{pmatrix}, \hat{C}_b = \begin{pmatrix} 0 & 0 & C & 0 \\ 0 & 0 & 0 & C \\ C & 0 & 0 & 0 \\ 0 & C & 0 & 0 \end{pmatrix}, \hat{C}_c = \begin{pmatrix} 0 & C & 0 & 0 \\ 0 & 0 & C & 0 \\ 0 & 0 & 0 & C \\ C & 0 & 0 & 0 \end{pmatrix}, \hat{C}_d = \begin{pmatrix} C & 0 & 0 & 0 \\ 0 & C & 0 & 0 \\ 0 & 0 & C & 0 \\ 0 & 0 & 0 & C \end{pmatrix}, \tag{8}$$

where C is the capacitance between two neighboring nodes. Then using Eq. (7), we have the effective coupling $t_a = iC$, $t_b = -C$, $t_c = -iC$, $t_d = C$. Therefore, the four subnode circuit can realize any arbitrary tight-binding model, with hopping phases corresponding to the fourth roots of unity, namely $\exp(2\pi im/4)$, with $m = 1, 2, 3, 4$, i.e., either purely real or purely imaginary.

This construction can now be further generalized to a hopping with phase $\theta_{n,m} = \exp(2i\pi(1-m)/n)$, with $m = 1, 2, ...n$, with are the nth roots of unity. In this case, each node contains n subnodes. The hopping elements are obtained by projecting the connectivity matrices onto the subspace spanned by the n-component vector $\hat{v}$, with the elements $\hat{v}_m = \theta_m$. The matrix corresponding to the "one-shift" in the connectivity $1 \to n$, $2 \to 1$, $3 \to 2$,..., $n \to n-1$, generates the hopping equal to $t_1 = \exp(2i\pi/n)$. More generally, an s-shift results in the hopping phase equal $t_s = \exp(2i\pi s/n)$.

Supplementary Note 4: Derivation of circuit Laplacian in the moment space

In this section, we give the detailed derivation of circuit laplacian matrix in the moment space in the experiment. Based on the Kirchhoff's law, the relationship between the node alternating current and voltage should satisfy the following equation:

$$I_\alpha = i\omega[-\sum_\beta \frac{V_\alpha - V_\beta}{\omega^2 L_{\alpha\beta}} - \frac{V_\alpha}{\omega^2 L_\alpha} + V_\alpha C_\alpha + \sum_\gamma C_{\alpha\gamma}(V_\alpha - V_\gamma)], \tag{9}$$

where I_α and V_α are the net current and voltage of node α with angular frequency being ω. $L_{\alpha\beta}$ is the inductance between node α and node β. C_α and L_α is the ground capacitance and inductance at node α. $C_{\alpha\gamma}$ is the capacitance between node α and node γ. The summation is taken over all nodes, which are connected to node α through an inductor or a capacitor.

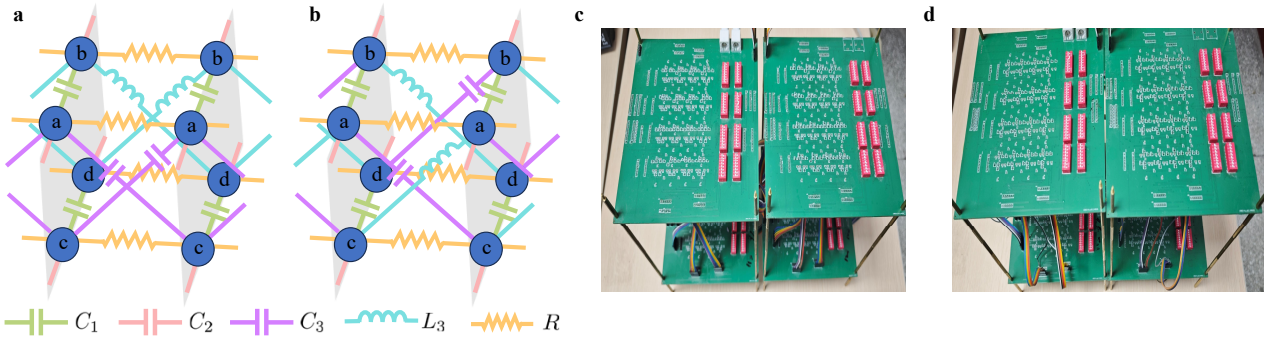

FIG. S6: The circuit-lattice mapping of two unit cells and the experimental circuit board for (a,c) $\theta = 0$ and (b,d) $\theta = \pm\pi$. Each node is grounded via inductance L_g, see Fig. S4 and Fig. S5.

To realize the model with different gauge field phase values ($\theta = 0, \pm 0.5\pi, \pm\pi$), we constructed three distinct circuit metamaterials, as illustrated in Fig. S6(a), Fig. 3(a) of the main text, and Fig. S6(b). For the $\theta = 0$ circuit, shown in Fig. S6(a), each site grounded through an inductor L_g is connected to other sites via four types of couplings: (i) intra-cell coupling through a capacitor C_1, (ii) inter-cell coupling through another capacitor C_2, (iii) two inter-cell dissipative couplings via resistors R, and (iv) two inter-layer couplings, with capacitors C_3 connecting sites a and c, and inductors L_3 connecting sites b and d.

$$\begin{bmatrix} I_a \\ I_b \\ I_c \\ I_d \end{bmatrix} = -i\omega\{\frac{1}{\omega^2 L_g}\begin{bmatrix} 1&0&0&0 \\ 0&1&0&0 \\ 0&0&1&0 \\ 0&0&0&1 \end{bmatrix} + C_1\begin{bmatrix} -1&1&0&0 \\ 1&-1&0&0 \\ 0&0&-1&1 \\ 0&0&1&-1 \end{bmatrix} + C_2\begin{bmatrix} -1&e^{ik_y}&0&0 \\ e^{-ik_y}&-1&0&0 \\ 0&0&-1&e^{ik_y} \\ 0&0&e^{-ik_y}&-1 \end{bmatrix} + C_3\begin{bmatrix} -2&0&2\cos k_x&0 \\ 0&-2&0&0 \\ 2\cos k_x&0&-2&0 \\ 0&0&0&-2 \end{bmatrix}$$
$$+\frac{1}{\omega^2 L_3}\begin{bmatrix} 2&0&0&0 \\ 0&2&0&-2\cos k_x \\ 0&0&2&0 \\ 0&-2\cos k_x&0&2 \end{bmatrix} + \frac{1}{i\omega R}\begin{bmatrix} -2+2\cos k_x&0&0&0 \\ 0&-2+2\cos k_x&0&0 \\ 0&0&-2+2\cos k_x&0 \\ 0&0&0&-2+2\cos k_x \end{bmatrix}\}\begin{bmatrix} V_a \\ V_b \\ V_c \\ V_d \end{bmatrix}. \tag{10}$$

We assume there are no external sources, meaning the current flowing out of each node is zero, i.e., $[I_a, I_b, I_c, I_d] = 0$. At the resonant frequency, $\omega_0 = 1/\sqrt{C_3 L_3} = 1/\sqrt{(C_1 + C_2)L_g}$ with $R = \frac{1}{\omega_0 C_3}$, the Laplacian matrix for the circuit

becomes:

$$J_{(0)}(\omega_0) = -i\omega_0\{-2iC_3(-1+\cos k_x)\sigma_0\tau_0 + (C_1 + C_2\cos k_y)\sigma_0\tau_x + C_2\sin k_y\sigma_0\tau_y + 2C_3\cos k_x\sigma_x\tau_z\}. \tag{11}$$

At resanont frequency ω_0, we find that the circuit Laplacian can recover the Hamiltonian by $J_{(0)}(\omega_0) = -iH_{(0)} + 2\omega_0 C_3$ (where $2\omega_0 C_3$ is a constant term that does not affect the results), with following one-to-one correspondence: $t_1 \Leftrightarrow \omega_0 C_1$, $t_2 \Leftrightarrow \omega_0 C_2$, $t_3 \Leftrightarrow \omega_0 C_3$. For this case, the parameters of the components used in our experiments are summarized in Table S1.

Supplemental Table I

	Electric elements	Mean value	tolerance	R_{DC}
C_1	YAGEO 0402 (50V)	22*nf*	±5%	
C_2	YAGEO 0603 (50V)	100*nf*	±5%	
C_3	YAGEO 0603 (50V)	50*nf*	±5%	
L_3	TDK 0805	44*uH*	±5%	0.9Ω
L_g	TDK 0805	18*uH*	±5%	0.38Ω
R	YAGEO 0603 (100mW)	30Ω	±0.1%	

TABLE S1: Electric elements used in the experiments for $\theta = 0$ include capacitors, inductors, and resistors. The capacitors from YAGEO are available in 0402 and 0603 packages, the low-resistance inductors from TDK are in the 0805 SMD package, and the resistors from YAGEO are in 0603. The resonant frequency of the circuit is $\omega_0 \approx 107.5$kHz and all circuit elements have a maximum tolerance is 5%.

For $\theta = \pm 0.5\pi$ circuit, as shown in Fig. 3(a) of the main text, each site consists of four nodes. The voltage and current at site i ($i = a, b, c, d$) are expressed as: $V_i = [V_{i,1}, V_{i,2}, V_{i,3}, V_{i,4}]^T$ and $I_i = [I_{i,1}, I_{i,2}, I_{i,3}, I_{i,4}]^T$, respectively. Each site (grounded via L_g) is connected to other sites through four types of couplings: (i) intra-cell coupling C_1, (ii) inter-cell coupling C_2, (iii) two inter-cell dissipative couplings R, and (iv) two inter-layer inter-cell couplings C_3. These inter-layer couplings also incorporate a gauge field phase θ. The Kirchhoff equation at each site can be written as:

$$\begin{aligned}
\begin{bmatrix} I_{a,1} \\ I_{a,2} \\ I_{a,3} \\ I_{a,4} \end{bmatrix} =& -i\omega\{C_0 \begin{bmatrix} -2 & 1 & 0 & 1 \\ 1 & -2 & 1 & 0 \\ 0 & 1 & -2 & 1 \\ 1 & 0 & 1 & -2 \end{bmatrix} \begin{bmatrix} V_{a,1} \\ V_{a,2} \\ V_{a,3} \\ V_{a,4} \end{bmatrix} + \frac{1}{\omega^2 L_g} \begin{bmatrix} V_{a,1} \\ V_{a,2} \\ V_{a,3} \\ V_{a,4} \end{bmatrix} - C_1 \begin{bmatrix} V_{a,1} - V_{b,1} \\ V_{a,2} - V_{b,2} \\ V_{a,3} - V_{b,3} \\ V_{a,4} - V_{b,4} \end{bmatrix} - C_2 \begin{bmatrix} V_{a,1} - e^{ik_y} V_{b,1} \\ V_{a,2} - e^{ik_y} V_{b,2} \\ V_{a,3} - e^{ik_y} V_{b,3} \\ V_{a,4} - e^{ik_y} V_{b,4} \end{bmatrix} \\
& - \frac{1}{i\omega R} \begin{bmatrix} V_{a,1} - e^{ik_x} V_{a,1} \\ V_{a,2} - e^{ik_x} V_{a,2} \\ V_{a,3} - e^{ik_x} V_{a,3} \\ V_{a,4} - e^{ik_x} V_{a,4} \end{bmatrix} - \frac{1}{i\omega R} \begin{bmatrix} V_{a,1} - e^{-ik_x} V_{a,1} \\ V_{a,2} - e^{-ik_x} V_{a,2} \\ V_{a,3} - e^{-ik_x} V_{a,3} \\ V_{a,4} - e^{-ik_x} V_{a,4} \end{bmatrix} - C_3 \begin{bmatrix} V_{a,1} - e^{-ik_x} V_{c,1} \\ V_{a,2} - e^{-ik_x} V_{c,2} \\ V_{a,3} - e^{-ik_x} V_{c,3} \\ V_{a,4} - e^{-ik_x} V_{c,4} \end{bmatrix} - C_3 \begin{bmatrix} V_{a,1} - e^{ik_x} V_{c,2} \\ V_{a,2} - e^{ik_x} V_{c,3} \\ V_{a,3} - e^{ik_x} V_{c,4} \\ V_{a,4} - e^{ik_x} V_{c,1} \end{bmatrix}\},
\end{aligned} \tag{12}$$

$$\begin{aligned}
\begin{bmatrix} I_{b,1} \\ I_{b,2} \\ I_{b,3} \\ I_{b,4} \end{bmatrix} =& -i\omega\{C_0 \begin{bmatrix} -2 & 1 & 0 & 1 \\ 1 & -2 & 1 & 0 \\ 0 & 1 & -2 & 1 \\ 1 & 0 & 1 & -2 \end{bmatrix} \begin{bmatrix} V_{b,1} \\ V_{b,2} \\ V_{b,3} \\ V_{b,4} \end{bmatrix} + \frac{1}{\omega^2 L_g} \begin{bmatrix} V_{b,1} \\ V_{b,2} \\ V_{b,3} \\ V_{b,4} \end{bmatrix} - C_1 \begin{bmatrix} V_{b,1} - V_{a,1} \\ V_{b,2} - V_{a,2} \\ V_{b,3} - V_{a,3} \\ V_{b,4} - V_{a,4} \end{bmatrix} - C_2 \begin{bmatrix} V_{b,1} - e^{-ik_y} V_{a,1} \\ V_{b,2} - e^{-ik_y} V_{a,2} \\ V_{b,3} - e^{-ik_y} V_{a,3} \\ V_{b,4} - e^{-ik_y} V_{a,4} \end{bmatrix} \\
& - \frac{1}{i\omega R} \begin{bmatrix} V_{b,1} - e^{ik_x} V_{b,1} \\ V_{b,2} - e^{ik_x} V_{b,2} \\ V_{b,3} - e^{ik_x} V_{b,3} \\ V_{b,4} - e^{ik_x} V_{b,4} \end{bmatrix} - \frac{1}{i\omega R} \begin{bmatrix} V_{b,1} - e^{-ik_x} V_{b,1} \\ V_{b,2} - e^{-ik_x} V_{b,2} \\ V_{b,3} - e^{-ik_x} V_{b,3} \\ V_{b,4} - e^{-ik_x} V_{b,4} \end{bmatrix} - C_3 \begin{bmatrix} V_{b,1} - e^{-ik_x} V_{d,3} \\ V_{b,2} - e^{-ik_x} V_{d,4} \\ V_{b,3} - e^{-ik_x} V_{d,1} \\ V_{b,4} - e^{-ik_x} V_{d,2} \end{bmatrix} - C_3 \begin{bmatrix} V_{b,1} - e^{ik_x} V_{d,4} \\ V_{b,2} - e^{ik_x} V_{d,1} \\ V_{b,3} - e^{ik_x} V_{d,2} \\ V_{b,4} - e^{ik_x} V_{d,3} \end{bmatrix}\},
\end{aligned} \tag{13}$$

$$\begin{aligned}
\begin{bmatrix} I_{c,1} \\ I_{c,2} \\ I_{c,3} \\ I_{c,4} \end{bmatrix} =& -i\omega\{C_0 \begin{bmatrix} -2 & 1 & 0 & 1 \\ 1 & -2 & 1 & 0 \\ 0 & 1 & -2 & 1 \\ 1 & 0 & 1 & -2 \end{bmatrix} \begin{bmatrix} V_{c,1} \\ V_{c,2} \\ V_{c,3} \\ V_{c,4} \end{bmatrix} + \frac{1}{\omega^2 L_g} \begin{bmatrix} V_{c,1} \\ V_{c,2} \\ V_{c,3} \\ V_{c,4} \end{bmatrix} - C_1 \begin{bmatrix} V_{c,1} - V_{d,1} \\ V_{c,2} - V_{d,2} \\ V_{c,3} - V_{d,3} \\ V_{c,4} - V_{d,4} \end{bmatrix} - C_2 \begin{bmatrix} V_{c,1} - e^{ik_y} V_{d,1} \\ V_{c,2} - e^{ik_y} V_{d,2} \\ V_{c,3} - e^{ik_y} V_{d,3} \\ V_{c,4} - e^{ik_y} V_{d,4} \end{bmatrix} \\
& - \frac{1}{i\omega R} \begin{bmatrix} V_{c,1} - e^{ik_x} V_{c,1} \\ V_{c,2} - e^{ik_x} V_{c,2} \\ V_{c,3} - e^{ik_x} V_{c,3} \\ V_{c,4} - e^{ik_x} V_{c,4} \end{bmatrix} - \frac{1}{i\omega R} \begin{bmatrix} V_{c,1} - e^{-ik_x} V_{c,1} \\ V_{c,2} - e^{-ik_x} V_{c,2} \\ V_{c,3} - e^{-ik_x} V_{c,3} \\ V_{c,4} - e^{-ik_x} V_{c,4} \end{bmatrix} - C_3 \begin{bmatrix} V_{c,1} - e^{-ik_x} V_{a,4} \\ V_{c,2} - e^{-ik_x} V_{a,1} \\ V_{c,3} - e^{-ik_x} V_{a,2} \\ V_{c,4} - e^{-ik_x} V_{a,3} \end{bmatrix} - C_3 \begin{bmatrix} V_{c,1} - e^{ik_x} V_{a,1} \\ V_{c,2} - e^{ik_x} V_{a,2} \\ V_{c,3} - e^{ik_x} V_{a,3} \\ V_{c,4} - e^{ik_x} V_{a,4} \end{bmatrix}\},
\end{aligned} \tag{14}$$

$$\begin{bmatrix} I_{d,1} \\ I_{d,2} \\ I_{d,3} \\ I_{d,4} \end{bmatrix} = -i\omega\{C_0 \begin{bmatrix} -2 & 1 & 0 & 1 \\ 1 & -2 & 1 & 0 \\ 0 & 1 & -2 & 1 \\ 1 & 0 & 1 & -2 \end{bmatrix} \begin{bmatrix} V_{d,1} \\ V_{d,2} \\ V_{d,3} \\ V_{d,4} \end{bmatrix} + \frac{1}{\omega^2 L_g} \begin{bmatrix} V_{d,1} \\ V_{d,2} \\ V_{d,3} \\ V_{d,4} \end{bmatrix} - C_1 \begin{bmatrix} V_{d,1} - V_{c,1} \\ V_{d,2} - V_{c,2} \\ V_{d,3} - V_{c,3} \\ V_{d,4} - V_{c,4} \end{bmatrix} - C_2 \begin{bmatrix} V_{d,1} - e^{-ik_y} V_{c,1} \\ V_{d,2} - e^{-ik_y} V_{c,2} \\ V_{d,3} - e^{-ik_y} V_{c,3} \\ V_{d,4} - e^{-ik_y} V_{c,4} \end{bmatrix}$$
$$- \frac{1}{i\omega R} \begin{bmatrix} V_{d,1} - e^{ik_x} V_{d,1} \\ V_{d,2} - e^{ik_x} V_{d,2} \\ V_{d,3} - e^{ik_x} V_{d,3} \\ V_{d,4} - e^{ik_x} V_{d,4} \end{bmatrix} - \frac{1}{i\omega R} \begin{bmatrix} V_{d,1} - e^{-ik_x} V_{d,1} \\ V_{d,2} - e^{-ik_x} V_{d,2} \\ V_{d,3} - e^{-ik_x} V_{d,3} \\ V_{d,4} - e^{-ik_x} V_{d,4} \end{bmatrix} - C_3 \begin{bmatrix} V_{d,1} - e^{-ik_x} V_{b,2} \\ V_{d,2} - e^{-ik_x} V_{b,3} \\ V_{d,3} - e^{-ik_x} V_{b,4} \\ V_{d,4} - e^{-ik_x} V_{b,1} \end{bmatrix} - C_3 \begin{bmatrix} V_{d,1} - e^{ik_x} V_{b,3} \\ V_{d,2} - e^{ik_x} V_{b,4} \\ V_{d,3} - e^{ik_x} V_{b,1} \\ V_{d,4} - e^{ik_x} V_{b,2} \end{bmatrix}\}. \quad (15)$$

Eq. (12-15) can be simplied as

$$\begin{bmatrix} I_{a,1} \\ I_{a,2} \\ I_{a,3} \\ I_{a,4} \end{bmatrix} = -i\omega\{C_0 \begin{bmatrix} -2 & 1 & 0 & 1 \\ 1 & -2 & 1 & 0 \\ 0 & 1 & -2 & 1 \\ 1 & 0 & 1 & -2 \end{bmatrix} \begin{bmatrix} V_{a,1} \\ V_{a,2} \\ V_{a,3} \\ V_{a,4} \end{bmatrix} + \left(\frac{1}{\omega^2 L_g} - C_1 - C_2 - 2C_3 - \frac{2}{i\omega R}\right) \begin{bmatrix} V_{a,1} \\ V_{a,2} \\ V_{a,3} \\ V_{a,4} \end{bmatrix}$$
$$+ \left(C_1 + C_2 e^{ik_y}\right) \begin{bmatrix} V_{b,1} \\ V_{b,2} \\ V_{b,3} \\ V_{b,4} \end{bmatrix} + \frac{2\cos k_x}{i\omega R} \begin{bmatrix} V_{a,1} \\ V_{a,2} \\ V_{a,3} \\ V_{a,4} \end{bmatrix} + C_3 e^{-ik_x} \begin{bmatrix} V_{c,1} \\ V_{c,2} \\ V_{c,3} \\ V_{c,4} \end{bmatrix} + C_3 e^{ik_x} \begin{bmatrix} V_{c,4} \\ V_{c,1} \\ V_{c,2} \\ V_{c,3} \end{bmatrix}\}, \quad (16)$$

$$\begin{bmatrix} I_{b,1} \\ I_{b,2} \\ I_{b,3} \\ I_{b,4} \end{bmatrix} = -i\omega\{C_0 \begin{bmatrix} -2 & 1 & 0 & 1 \\ 1 & -2 & 1 & 0 \\ 0 & 1 & -2 & 1 \\ 1 & 0 & 1 & -2 \end{bmatrix} \begin{bmatrix} V_{b,1} \\ V_{b,2} \\ V_{b,3} \\ V_{b,4} \end{bmatrix} + \left(\frac{1}{\omega^2 L_g} - C_1 - C_2 - 2C_3 - \frac{2}{i\omega R}\right) \begin{bmatrix} V_{b,1} \\ V_{b,2} \\ V_{b,3} \\ V_{b,4} \end{bmatrix}$$
$$+ \left(C_1 + C_2 e^{-ik_y}\right) \begin{bmatrix} V_{a,1} \\ V_{a,2} \\ V_{a,3} \\ V_{a,4} \end{bmatrix} + \frac{2\cos k_x}{i\omega R} \begin{bmatrix} V_{b,1} \\ V_{b,2} \\ V_{b,3} \\ V_{b,4} \end{bmatrix} + C_3 e^{-ik_x} \begin{bmatrix} V_{d,3} \\ V_{d,4} \\ V_{d,1} \\ V_{d,2} \end{bmatrix} + C_3 e^{ik_x} \begin{bmatrix} V_{d,2} \\ V_{d,3} \\ V_{d,4} \\ V_{d,1} \end{bmatrix}\}, \quad (17)$$

$$\begin{bmatrix} I_{c,1} \\ I_{c,2} \\ I_{c,3} \\ I_{c,4} \end{bmatrix} = -i\omega\{C_0 \begin{bmatrix} -2 & 1 & 0 & 1 \\ 1 & -2 & 1 & 0 \\ 0 & 1 & -2 & 1 \\ 1 & 0 & 1 & -2 \end{bmatrix} \begin{bmatrix} V_{c,1} \\ V_{c,2} \\ V_{c,3} \\ V_{c,4} \end{bmatrix} + \left(\frac{1}{\omega^2 L_g} - C_1 - C_2 - 2C_3 - \frac{2}{i\omega R}\right) \begin{bmatrix} V_{c,1} \\ V_{c,2} \\ V_{c,3} \\ V_{c,4} \end{bmatrix}$$
$$+ \left(C_1 + C_2 e^{ik_y}\right) \begin{bmatrix} V_{d,1} \\ V_{d,2} \\ V_{d,3} \\ V_{d,4} \end{bmatrix} + \frac{2\cos k_x}{i\omega R} \begin{bmatrix} V_{c,1} \\ V_{c,2} \\ V_{c,3} \\ V_{c,4} \end{bmatrix} + C_3 e^{-ik_x} \begin{bmatrix} V_{a,2} \\ V_{a,3} \\ V_{a,4} \\ V_{a,1} \end{bmatrix} + C_3 e^{ik_x} \begin{bmatrix} V_{a,1} \\ V_{a,2} \\ V_{a,3} \\ V_{a,4} \end{bmatrix}\}, \quad (18)$$

$$\begin{bmatrix} I_{d,1} \\ I_{d,2} \\ I_{d,3} \\ I_{d,4} \end{bmatrix} = -i\omega\{C_0 \begin{bmatrix} -2 & 1 & 0 & 1 \\ 1 & -2 & 1 & 0 \\ 0 & 1 & -2 & 1 \\ 1 & 0 & 1 & -2 \end{bmatrix} \begin{bmatrix} V_{d,1} \\ V_{d,2} \\ V_{d,3} \\ V_{d,4} \end{bmatrix} + \left(\frac{1}{\omega^2 L_g} - C_1 - C_2 - 2C_3 - \frac{2}{i\omega R}\right) \begin{bmatrix} V_{d,1} \\ V_{d,2} \\ V_{d,3} \\ V_{d,4} \end{bmatrix}$$
$$+ \left(C_1 + C_2 e^{-ik_y}\right) \begin{bmatrix} V_{c,1} \\ V_{c,2} \\ V_{c,3} \\ V_{c,4} \end{bmatrix} + \frac{2\cos k_x}{i\omega R} \begin{bmatrix} V_{d,1} \\ V_{d,2} \\ V_{d,3} \\ V_{d,4} \end{bmatrix} + C_3 e^{-ik_x} \begin{bmatrix} V_{b,4} \\ V_{b,1} \\ V_{b,2} \\ V_{b,3} \end{bmatrix} + C_3 e^{ik_x} \begin{bmatrix} V_{b,3} \\ V_{b,4} \\ V_{b,1} \\ V_{b,2} \end{bmatrix}\}. \quad (19)$$

Considering two distinct vectors $\hat{v}_1 = \frac{1}{2}[1, -i, -1, i]^T$ and $\hat{v}_2 = \frac{1}{2}[1, i, -1, -i]^T$, the corresponding new basis vectors are given by: $V'_{i,1} = V_{i,1} - iV_{i,2} - V_{i,3} + iV_{i,4}$ and $V'_{i,2} = V_{i,1} + iV_{i,2} - V_{i,3} - iV_{i,4}$, respectively. At the resonant frequency $\omega_0 = 1/\sqrt{(C_1 + C_2 + 2C_3 + 2C_0)L_g}$ and $R = \frac{1}{\omega_0 C_3}$. The original system of equations (Eq. (16-19)) can be separated into two independent Laplacian matrices. These two matrices represent the system in the new basis formed by $\hat{v}_1$ and $\hat{v}_2$:

$$J_{(0.5\pi)}(\omega_0) = -i\omega_0\{-2iC_3(-1 + \cos k_x)\sigma_0\tau_0 + (C_1 + C_2\cos k_y)\sigma_0\tau_x + C_2 \sin k_y \sigma_0\tau_y$$
$$+ C_3(\sin k_x - \cos k_x)\sigma_y\tau_z + C_3(\cos k_x - \sin k_x)\sigma_x\tau_z\}, \quad (20)$$
$$J_{(-0.5\pi)}(\omega_0) = -i\omega_0\{-2iC_3(-1 + \cos k_x)\sigma_0\tau_0 + (C_1 + C_2\cos k_y)\sigma_0\tau_x + C_2 \sin k_y \sigma_0\tau_y$$
$$+ C_3(\sin k_x + \cos k_x)\sigma_y\tau_z + C_3(\cos k_x + \sin k_x)\sigma_x\tau_z\}. \quad (21)$$

Similarly, the circuit Laplacian can recover the Hamiltonian through the relation $J_{(\pm 0.5\pi)}(\omega) = -iH_{(\pm 0.5\pi)} + 2\omega_0 C_3$ at resonant frequency ω_0, with a one-to-one correspondence between the parameters: $t_1 \Leftrightarrow \omega_0 C_1$, $t_2 \Leftrightarrow \omega_0 C_2$, $t_3 \Leftrightarrow \omega_0 C_3$. The specific values of the components used in our experiments are summarized in Table S2.

Supplemental Table II

	Electric elements	Mean value	tolerance	R_{DC}
C_0	YAGEO 0603 (50V)	2.2*nf*	±1%	
C_1	YAGEO 0603 (50V)	4.4*nf*	±1%	
C_2	FH 0805 (50V)	20*nf*	±5%	
C_3	YAGEO 0603 (50V)	10*nf*	±5%	
L_g	TDK 0805	44*uH*	±5%	0.9Ω
R	RESI 0805 (130mW)	146.5Ω	±0.1%	

TABLE S2: For $\theta = \pm 0.5\pi$, the experimental setup utilizes capacitors, inductors, and resistors. The capacitors, sourced from YAGEO or FH, are available in 0603 and 0805 packages. The low-resistance inductors from TDK and the resistors from RESI both use the 0805 package. The circuit operates at a resonant frequency of approximately $\omega_0 \approx 108$kHz, with all components ensuring a maximum tolerance of 5%.

For $\theta = \pm\pi$ circuit, as shown in Fig. S6(b), each site ground through an inductor L_g is connected with other sites through four kinds of coupling: (i) intra-cell coupling C_1, (ii) inter-cell coupling C_2, (iii) two dissipative inter-cell couplings R, and (iv) two inter-cell couplings between layers C_3 and L_3. The Kirchhoff equations for each site can be written as:

$$\begin{bmatrix} I_a \\ I_b \\ I_c \\ I_d \end{bmatrix} = -i\omega\{\frac{1}{\omega^2 L_g}\begin{bmatrix} 1&0&0&0 \\ 0&1&0&0 \\ 0&0&1&0 \\ 0&0&0&1 \end{bmatrix} + C_1\begin{bmatrix} -1&1&0&0 \\ 1&-1&0&0 \\ 0&0&-1&1 \\ 0&0&1&-1 \end{bmatrix} + C_2\begin{bmatrix} -1&e^{ik_y}&0&0 \\ e^{-ik_y}&-1&0&0 \\ 0&0&-1&e^{ik_y} \\ 0&0&e^{-ik_y}&-1 \end{bmatrix} + C_3\begin{bmatrix} -1&0&e^{-ik_x}&0 \\ 0&-1&0&e^{ik_x} \\ e^{ik_x}&0&-1&0 \\ 0&e^{-ik_x}&0&-1 \end{bmatrix}$$
$$+\frac{1}{\omega^2 L_3}\begin{bmatrix} 1&0&-e^{ik_x}&0 \\ 0&1&0&-e^{-ik_x} \\ -e^{-ik_x}&0&1&0 \\ 0&-e^{ik_x}&0&1 \end{bmatrix} + \frac{1}{i\omega R}\begin{bmatrix} -2+2\cos k_x&0&0&0 \\ 0&-2+2\cos k_x&0&0 \\ 0&0&-2+2\cos k_x&0 \\ 0&0&0&-2+2\cos k_x \end{bmatrix}\}\begin{bmatrix} V_a \\ V_b \\ V_c \\ V_d \end{bmatrix}. \tag{22}$$

Considering resonant frequency $\omega_0 = 1/\sqrt{C_3 L_3} = 1/\sqrt{(C_1+C_2)L_g}$ and $R = \frac{1}{\omega_0 C_3}$, the Laplacian matrix under these conditions becomes:

$$J_{(\pm\pi)}(\omega_0) = -i\omega_0\{-2iC_3(-1+\cos k_x)\sigma_0\tau_0 + (C_1 + C_2\cos k_y)\sigma_0\tau_x + C_2 \sin k_y \sigma_0\tau_y + 2C_3 \sin k_x \sigma_y\tau_z\}. \tag{23}$$

At resonant frequency ω_0, the circuit Laplacian can recover the Hamiltonian through the relation $J_{(\pm\pi)}(\omega_0) = -iH_{(\pm\pi)} + 2\omega_0 C_3$. In this case, we choose the parameters of the components same with $\theta = 0$.

Supplementary Note 5: Experimental details

In this section, we discuss the details of measuring the spin-dependent transmission coefficient. The opposite spin modes (spin-up and spin-down) are obtained by recombining the measured fields of the top and bottom layers. For the gauge field phase $\theta = \pi$, the eigenmodes of mirror symmerty $\mathcal{M}_z = -\sigma_y\tau_0$ are

$$|+\rangle_1 = \frac{1}{\sqrt{2}}\begin{bmatrix} 1 \\ 0 \\ -i \\ 0 \end{bmatrix}; |+\rangle_2 = \frac{1}{\sqrt{2}}\begin{bmatrix} 0 \\ 1 \\ 0 \\ -i \end{bmatrix}; |-\rangle_1 = \frac{1}{\sqrt{2}}\begin{bmatrix} 1 \\ 0 \\ i \\ 0 \end{bmatrix}; |-\rangle_2 = \frac{1}{\sqrt{2}}\begin{bmatrix} 0 \\ 1 \\ 0 \\ i \end{bmatrix}; \tag{24}$$

with eigenvalue $\{\pm 1\}$, respectively. We refer to the eigenvector spaces $\{|+\rangle_1, |+\rangle_2\}$ and $\{|-\rangle_1, |-\rangle_2\}$ as the spin-up and spin-down subspaces, respectively. By exciting the corresponding subnodes $S_\pm = S_1 \mp iS_2$, where S_1 and S_2 are subnodes of the top and bottom layers, we can get the spin-dependent transmission coefficient.

Similarly, for gauge field phase $\theta = 0$, the eigenmodes of mirror symmerty $\mathcal{M}_z = \sigma_x \tau_0$ are

$$|+\rangle_1 = \begin{bmatrix} 1 \\ 0 \\ 1 \\ 0 \end{bmatrix}; |+\rangle_2 = \begin{bmatrix} 0 \\ 1 \\ 0 \\ 1 \end{bmatrix}; |-\rangle_1 = \begin{bmatrix} 1 \\ 0 \\ -1 \\ 0 \end{bmatrix}; |-\rangle_2 = \begin{bmatrix} 0 \\ 1 \\ 0 \\ -1 \end{bmatrix}. \tag{25}$$

In this case, the spin-up and spin-down transmission coefficients are given by $S_\pm = S_1 \pm S_2$.

To ensure that the circuits under open boundary conditions still respect symmetry, the grounding for boundary and bulk units differs. This is due to the absence of off-diagonal circuit Laplacian elements at the boundary that connect other sites, which requires a reconfiguration of the grounding condition. To ensure the diagonal elements vanishing at the resonant frequency, the grounding settings for $\theta = 0,\ \pm 0.5\pi$ and $\pm\pi$ are respectively shown in Fig. S7.

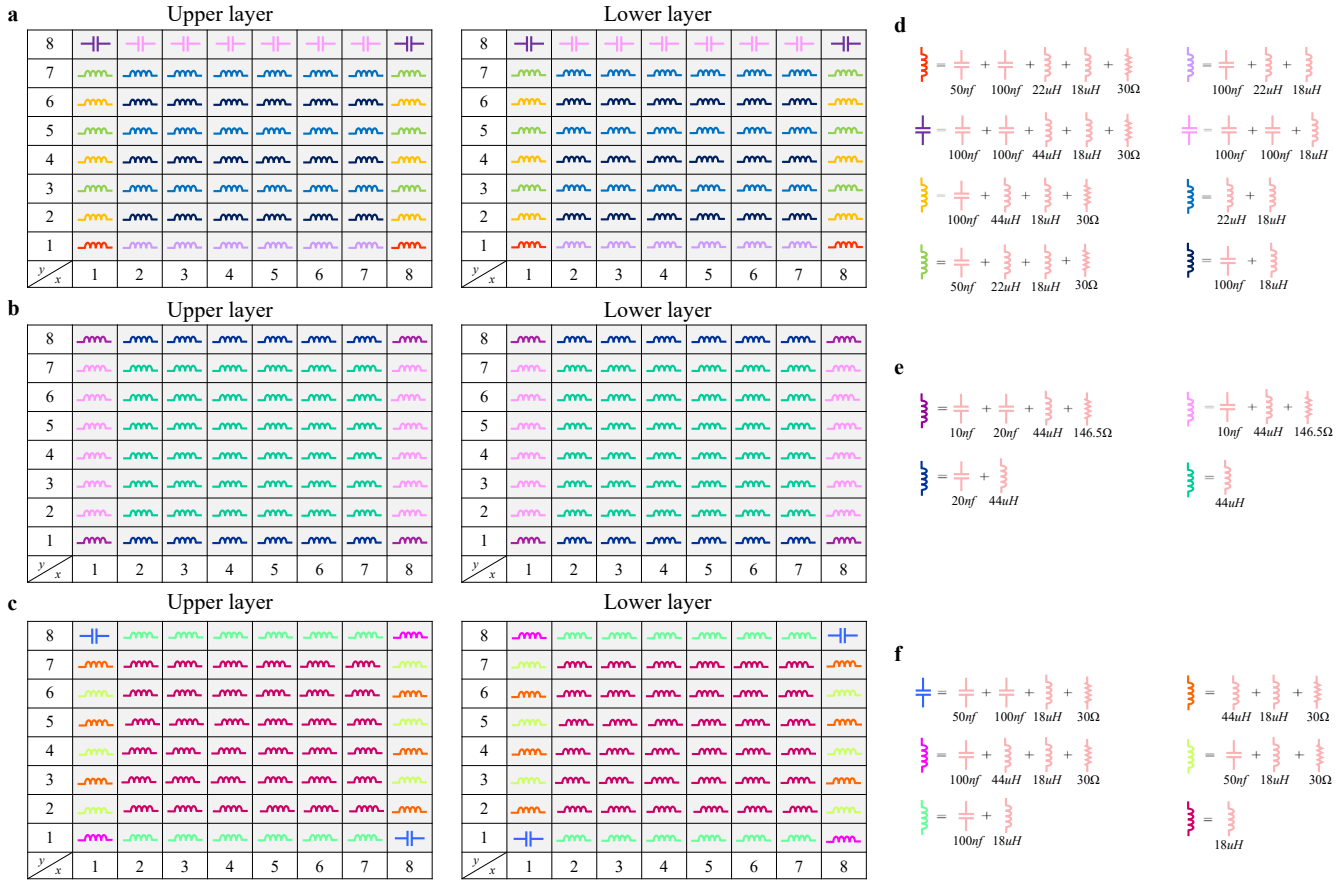

FIG. S7: The grounding settings for the upper layer (left panel) and lower layer (right panel) with gauge field phases (a) $\theta = 0$, (b) $\theta = \pm 0.5\pi$, and (c) $\theta = \pm\pi$. (d-f) The corresponding grounding elements used for $\theta = 0,\ \pm 0.5\pi,\ \pm\pi$.